Journal of Zhejiang University-SCIENCE A in press
www.jzus.zju.edu.cn; www.springer.com/journal/11582
E-mail: jzus_a@zju.edu.cn

Research Article
https://doi.org/10.1631/jzus.A2500379

A two-photon polymerization based microfluidic biochip incorporating a herringbone microchannel and deterministic lateral displacement design for efficient capture of circulating tumor cells

Xinyi LIANG[1,2*], Changwei QIN[1,2*], Kaiqiang LI[3], An REN[1,2], Jiarui HU[1,2], Weikang LV[1,2], Lunan KE[1,2], Zhen WANG[3], Mengfei YU[4], Xiuxiu JIANG[5], Huayong YANG[1,2], Xiaobin XU[6]✉, Liang MA[1,2]✉

[1]*State Key Laboratory of Fluid Power and Mechatronic Systems, Zhejiang University, Hangzhou 310058, China*
[2]*School of Mechanical Engineering, Zhejiang University, Hangzhou 310058, China*
[3]*Center for Laboratory Medicine, Allergy center, Department of Transfusion medicine, Zhejiang Provincial People's Hospital, Affiliated People's Hospital, Hangzhou Medical College, Hangzhou 310014, China*
[4]*The Affiliated Stomatologic Hospital, School of Medicine, Zhejiang University, Hangzhou 310003, China*
[5]*Zhejiang Provincial Clinical Research Center for Gynecology, Zhejiang Key Laboratory of Maternal and Infant Health, Department of Family Planning, Women's Hospital, Zhejiang University School of Medicine, Hangzhou 310006, China*
[6]*School of Materials Science of Engineering, Tongji University, Shanghai 201804, China*

Unedited

Abstract: Circulating tumor cells (CTCs) are cells that become detached from a primary tumor and enter the vascular or lymphatic system. These cells contain nearly the entire genetic information of the primary tumor. Enrichment and detection of CTCs play a crucial role in prognostications and risk assessments of tumor metastasis and recurrence, evaluation of efficacy and potential medications for precision tumor therapy, and detection of dynamic biomarkers during tumor treatment. Current methods of CTC capture often face the challenge of balancing capture rate and purity. To address these issues, we propose a microfluidic biochip based on the principle of immunoaffinity, which incorporates a herringbone microchannel and deterministic lateral displacement (DLD) technology for the capture of CTCs. By manipulating the internal structural design of the microfluidic chip, we optimized the flow field within the chip, thereby enhancing the contact frequency between cells and aptamers, and ultimately improving the capture rate. The proposed chip demonstrated a capture efficiency of approximately 91.87% for human breast cancer cells (MCF7), with a release rate of 77.5%. The relative viability of the released cells was approximately 94.08%. Notably, the specificity of the aptamers towards tumor cell surface antigens enables high-purity capture. Additionally, the use of DNA enzymes to digest aptamers facilitates the release of high-activity CTCs, offering a method to simultaneously achieve high capture rate, purity, and activity enrichment.

Key words: Circulating tumor cell; Cell sorting; Microfluidic chip

1 Introduction

Cancer is one of the leading threats to human longevity(Sung et al., 2021). In patients with cancer, some tumor cells become detached from the primary tumor, enter the circulatory system, and then travel throughout the body, where they may infiltrate normal tissues to colonize and form new tumors. This process is known as cancer metastasis. Cancer metastasis includes four processes: local invasion, endoinfiltration, exosmosis, and colonization, which is responsible for up to 90% of cancer deaths (Chaffer and Weinberg, 2011; Li et al., 2024). Detached tumor cells are also called Circulating Tumor Cells (CTCs) (Alix-Panabières and Pantel, 2014; Shu et al., 2024). Enrichment and detection of CTCs in peripheral blood is of great significance for early tumor diagnosis, prognosis and risk assessment of metastasis and recurrence (Cristofanilli et al., 2004; Cohen et al., 2006; De Bono et al., 2009), efficacy

✉ Liang MA: liangma@zju.edu.cn
Xiaobin XU: xiaobinxu@tongji.edu.cn
* The two authors contributed equally to this work
Liang MA, https://orcid.org/0000-0002-6242-1850

Received Aug. 8, 2025; Revision accepted Nov. 3, 2025; Crosschecked

© Zhejiang University Press 2025

evaluation and medication guidance regarding tumor precision therapy (Cortés-Hernández et al., 2020; Liu et al., 2023), and monitoring of dynamic markers during tumor therapy (Smerage et al., 2014; Ma and Yang, 2023).

The scarcity and heterogeneity of CTCs present substantial challenges to the enrichment, isolation, and subsequent detection of CTCs from blood samples. Existing circulating tumor cell capture techniques can be roughly divided into two categories: physics-based capture, and immune-binding capture (Kang et al., 2022; Liu et al., 2022; Hu et al., 2025).

Physics-based capture is mainly based on the differences in certain physical properties (such as size, density, deformations, dielectric properties, etc.) of CTCs and blood cells. It includes methods such as centrifugal separation (Rosenberg et al., 2002; Low and Abas, 2015), filtration separation (Sarioglu et al., 2015; Kang et al., 2017; Zhang et al., 2018; Chen et al., 2024), fluid mechanical separation (Zeming et al., 2013; Park et al., 2016; Renier et al., 2017; Salafi et al., 2019; Xiang et al., 2019), dielectrophoresis separation (Varmazyari et al., 2022; Wu et al., 2023), and acoustic electrophoresis separation (Antfolk et al., 2017; Wu et al., 2018). For instance, Rosenberg et al. showed that both the OnceQuick and Ficoll systems achieved a capture efficiency of 70%-90% when separating rectal cancer cells HT-29 from blood (Rosenberg, et al., 2002). Moreover, Kang captured nine different types of cancer cells using filters with conical slits, with an average capture rate of 77.7%; a vitality of 80.6% was also maintained for the cells (Kang, et al., 2017). However, such physical capture methods generally possess shortcomings of low capture rate, low capture purity, and low cell activity following capture.

The immune binding method uses certain molecules (antibodies or aptamers) to bind specifically to the surface antigens of cancer cells in order to capture CTCs (Sheng et al., 2013; Galletti et al., 2014; Zhou and Rossi, 2017; Shi et al., 2022; Kang et al., 2025). Considering the differences in the grafted surfaces of antibodies or aptamers, this method can be roughly divided into two categories: immunomagnetic separation, and functionalized micro-nano structure separation. Yu et al. affixed antibody-modified iron (III) oxide nanoparticles on nickel microcolumns using a magnetic field to fabricate a circulating tumor cell capture chip, which can separate out CTCs by simply removing the magnetic field (Yu et al., 2013). Also, Zhang et al. functionalized antibodies against horizontally stacked electrospun titanium dioxide nanofibers for the capture of CTCs (Zhang et al., 2012), and increased the capture rate by utilizing the interaction between the substrate and the extracellular matrix surface. CTC capture techniques based on immune binding tend to require a longer incubation period to induce cell binding to antibodies or aptamers, resulting in lower fluxes. Meanwhile, some antibody-based capture methods can release tumor cells through proteolytic hydrolysis of antibodies, which will affect the activity of tumor cells and the number of membrane proteins; this complicates subsequent analysis of tumor cells.

In order to overcome the limitations of existing CTC capture technologies – namely low capture rate, low purity, and insufficient activity of the captured CTCs – a microfluidic chip based on the immune binding principle which leverages a herringbone-shaped microchannel and deterministic lateral displacement technology was proposed. Using the advanced two-photon-polymerization fabrication method, the bottom capture unit can be fabricated with high resolution with high reproducibility. Moreover, by influencing the flow field inside the chip (Lin et al., 2023), the contact frequency between cells and aptamers can be increased, and the capture rate improved. The specificity of aptamers to tumor cell surface antigens is used to achieve high purity capture. The digestion of aptamers by DNase is also leveraged to promote high activity release of the captured CTCs.

2 Materials and methods

The content of this paper mainly consists of three parts: first, structural design of the top herringbone-shaped microchannel and the bottom column is performed, then the designed chip is processed and the aptamer is modified, and finally the capture experiment is conducted to verify the effectiveness of the simulation and explore the optimal operational parameters of the chip. Following this research content, the overall framework is

Unedited

illustrated in Fig. 1.

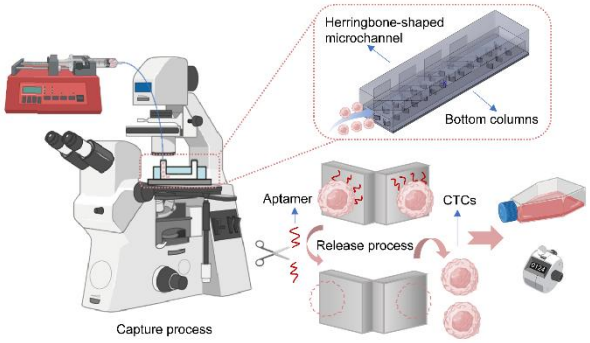

Fig. 1 A schematic of the CTC capture system

2.1 Materials

An SU-8-3050 photoresist was purchased from MicroChem (USA). Polydimethylsiloxane was obtained from Dow Corning (USA). An IP-Dip2 photoresist was supplied by NanoScribe (Germany). A Cell Tracker Red CMTPX and a Cell Tracker Green CMFDA were purchased from ThermoFisher (USA). (3-Mercaptopropyl) trimethoxysilane (MPTS), propylene glycol monomethyl ether acetate (PGMEA), and 4-maleimidobutyric acid N-hydroxysuccinimide ester (GMBS) were purchased from Aladdin (China). Streptavidin, Alexa Fluor 680-labeled streptavidin, DAPI solution, Tween-20, bovine serum albumin (BSA), and red blood cell lysis buffer were obtained from Solarbio (China). Human breast cancer cell line MCF-7 and human chronic myeloid leukemia cell line K562 (both with complete mediums) were purchased from Saibaikang (China). FITC-labeled phalloidin was supplied by Yisheng (China). Recombinant deoxyribonuclease I, mouse-derived recombinant EpCAM antibody, and Cy5-labeled goat anti-mouse IgG were purchased from Saivier (China). The biotinylated SYL3C aptamer and Cy5-labeled aptamer were synthesized by Tsingke Biotechnology Co., Ltd. (China).

2.2 Chip fabrication

The top structure of the chip was constructed using soft lithography technology that is common for microfluidic devices. In short, the SU-8 mold was first engraved, and then the top herringbone-shaped microchannel was constructed using PDMS reverse molding and drilling. The bottom structure was established through a two-photon polymerization (TPP) method using a 3D TPP printer (PPGT2, Nanoscribe, Germany) with its 3D SF Dill module (63-fold objective) and IP-Dip2 photoresist. The 3D model was built using Solidworks, was sliced using Describe software (version 2.7) after completion, and the output GWL file was imported into Nanowrite (version 1.10.5 ） software for printing. The microstructure is then printed on silylated fused quartz glass with a glass size of 75 mm × 25 mm × 1 mm. The quartz glass with the top PDMS and the bottom printed with the microstructure was treated with oxygen plasma 50 W for 30 s, and subsequently the assembly was completed through alignment and pressing under an industrial microscope.

2.3 Aptamer modification

The aptamer modification process was performed following the manufacturer's instructions. To summarize, anhydrous ethanol solution of 5%v/v MPTS was injected into the chip and incubated at room temperature for 30 min to graft the sulfhydryl groups. After rinsing with anhydrous ethanol, 10 mM GMBS anhydrous ethanol solution was injected and incubated at room temperature for 30 min to graft the NHS ester. Also following this rinsing, 50 μg/mL of streptavidin was injected and incubated overnight. Finally, the modification was completed after rinsing with PBS and injecting 1.5 μM biotinylated aptamer with a 2 h incubation time.

2.4 Tumor cell culture

The tumor cell lines were cultured in the corresponding complete medium in a 37 ℃ incubator with 5% carbon dioxide. EpCAM positive human breast cancer cell line MCF-7 was used as the model's CTC, and EpCAM negative human chronic myeloid leukemia cell line K562 was used as the model's leukocyte.

2.5 Cell capture and release

Before the capture experiment, live cells were stained with 1 μM Cell Tracker Red CMTPX or Cell Tracker Green CMFDA to facilitate follow-up observations and counting. To prepare the cell suspension for capture, MCF-7 was first digested with pancreatic enzyme-free cell digestion solution, the

Unedited

supernatant was discarded after centrifugation, and then resuspension was performed with phenol-free red DMEM. For suspension cell K562, the digestion step can be omitted. The cells were counted using a hemocytometer, and specific cell concentrations of MCF-7 and K562 single cell or mixed cell suspensions were prepared using gradient dilution. The suspension was then extracted into a 1 mL syringe and injected into the microfluidic chip with an injection pump at a constant flow rate. Subsequently, 500 μL of PBS buffer was injected to flush out the uncaptured cells, and subsequent counting and other operations were performed.

After the capture and flushing process, the captured cells were counted under an inverted fluorescence microscope. Considering the number of the captured cells for N_1 and the total number of cells N, the capture rate R_c can be calculated as:

$$R_c = \frac{N_1}{N} \times 100\%, \quad (1)$$

Cell release was performed using Recombinant deoxyribonuclease I by first combining Recombinant DNase I, dilutive solution, and ultrapure water in 1 U: 1 μL: 10 μL. Then the working liquid was injected into the chip and incubated at 37 ℃ in the incubator for half an hour. Thereafter, 2 mL of phenol-free red DMEM was injected into the chip to flush out the released cells. The cells that were not released were counted under an inverted fluorescence microscope. With the number of cells which are not released being N_2, the release rate R_r can be calculated as:

$$R_r = \frac{N_1 - N_2}{N_1} \times 100\%, \quad (2)$$

2.6 Statistical analysis

All data were presented as mean ± standard deviation (SD) values from at least three independent experiments. The statistical difference between the control group and the experimental group was assessed using the independent samples t-test. All analyses and plotting were performed using Origin (Version 2024, OriginLab Co., USA). A p-value less than 0.05 was considered statistically significant.

3 Results and discussion

3.1 Chip top structural design

The top structure of the CTC capture chip was constructed as a herringbone-shaped microchannel. The herringbone-shaped mixer is simple and easy to manufacture, and is commonly used in microfluidics. Micro-vortexes can be generated in the microchannel, promote the diffusion of the fluid through the stretching and folding of the fluid volume, and achieve mixing of various fluids. Applying the herringbone-shaped mixer in the capture of CTCs can increase the frequency of cell collisions with the wall, and thus increase the capture rate.

The basic size of the herringbone-shaped microchannel structure is shown in Fig. 2(a). The dimensions of the microchannel are described by the minimum element width ω, asymmetry p_1, runner height h, height αh, width ω_1, spacing d, and deflection angles α_1 and α_2.

The size parameters of the herringbone mixer were set according to existing studies. For instance, Stroock's research showed that when $\alpha_1 = \alpha_2 = 45°$, $\frac{2\pi\alpha h}{\omega_1+d} \sim 2$, the herringbone mixer showed the greatest transverse flow (that is, the ratio of transverse to axial flow) (Stroock et al., 2002). Therefore we take $\alpha_1 = \alpha_2 = 45°$, $\frac{2\pi\alpha h}{\omega_1+d} \sim 2$. Moreover, a simulation study by Li showed that a herringbone asymmetry of 0.6 displayed the greatest transverse flow (Li and Chen, 2005). Thus we set the asymmetry degree of the herringbone-shaped microchannel to 0.6.

High susceptibility to clogging is a common problem in microfluidic chips used for CTC capture. To address this, we must design the flow path height to accommodate the size of the CTCs. CTCs are 15-40 μm in diameter, and thus the flow channel height needs to be above 40 μm. But for the sake of more accurate control of the fluid and cell movement in the channel, the flow height should not be too large. Therefore, the flow channel height is set at 50 μm. The preliminary design of the herringbone-shaped microchannel is summarized in Table 1, and simulation design is only needed for ω, ω_1, and d. The purpose of the top herringbone design is to promote frequent contact between the fluid and the cells within the fluid and the wall. Accordingly, the

Unedited

target physical quantity was the average flow velocity v_{yz} perpendicular to the mainstream directional plane, which is the volume fraction of v_{yz}.

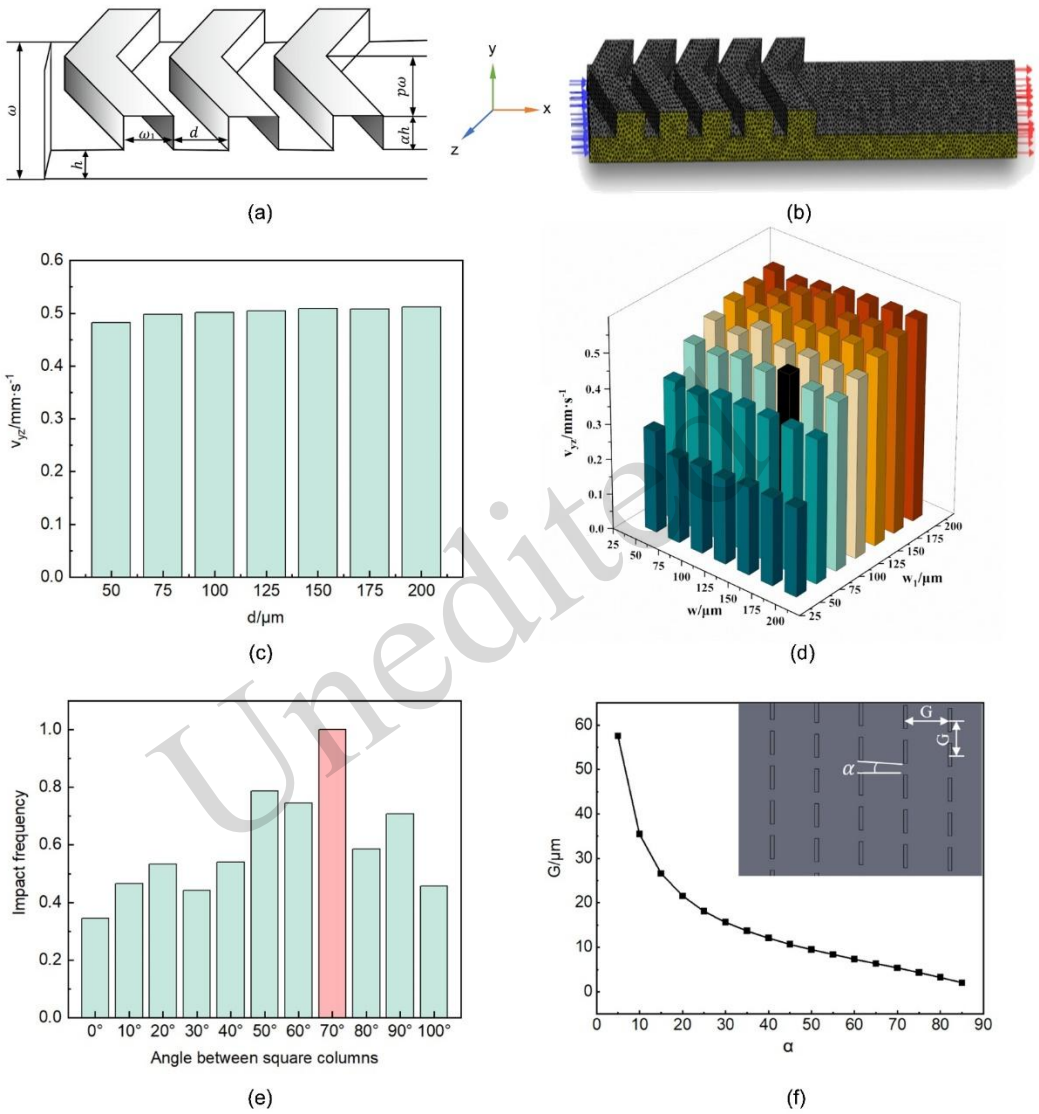

Fig. 2 Chip structure design and optimization. (a) Diagram of the basic dimensions of the herringbone-shaped structure; (b) Mesh diagram; (c) The relationship between v_{yz} and the herringbone-shaped spacing d; (d) The relationship between v_{yz} and the herringbone-shape width and minimum element width; (e) The relationship between the angle of square column and the collision frequency; (f) Schematic diagram of the column parameters and the relationship between spacing and offset angle.

Table 1 Preliminary restrictions on the basic dimensions of the herringbone shape

Parameters	Dimensions	Basis of determination
α_1 α_2	45°	Ref.(Stroock, et al., 2002)
α	$\frac{2\pi\alpha h}{\omega_1 + d} \sim 2$	
ω_1		
p_1	0.6	Ref.(Li and Chen, 2005)
h	$50\mu m$	Determined by the size of the CTCs and their movement within the

Unedited

		fluid.
d	undetermined	
ω	undetermined	

First, the herringbone spacing d was designed. The size ranges needed to be delineated at an early stage of the design process. If the herringbone shape spacing is too small, it will cause difficulties in fabrication, so the minimum value of the spacing was set as 50 μm, the maximum was 200 μm, and the gradient was 25 μm. The minimum element width of the fixed herringbone shape is 150 μm, and the herringbone shape width is 100 μm. The simulations of the relationship of v_{yz} with d are shown in Fig. 2(c). It can be observed that with the increase of d, the change in v_{yz} is very small; thus in order to increase the number of vortices, the number of herringbone grooves should be increased. Hence, the herringbone spacing was set at a smaller value of 50 μm.

After determining the herringbone spacing d, there are only two remaining parameters, ω and ω_1, to be optimized. First, we need to determine their size limits in order to constrain the simulation optimization. If the minimum element width ω is too small, it will increase the aspect ratio of the structure, which is not conducive to developing and engraving. Therefore, the minimum for the size range of ω is determined to be 50 μm – consistent with the height of the flow channel. If ω is too large, the total number of vortices will be slightly reduced, so the maximum size was set as 200 μm and the gradient was set as 25 μm. The size range and gradient of the herringbone width ω_1 are the same as for the minimum element width ω. Using the size range and gradient of the two models, 49 flow-domain models were established. The relationship between the simulated v_{yz} and the minimum cell width ω and herringbone width ω_1 is shown in the three-dimensional bar chart in Fig. 2(d).

It can be seen in Fig. S1(a) that when the minimum element width ω is fixed, with increasing herringbone width ω_1, the average flow velocity perpendicular to the main flow plane increases rapidly at first, and then slows. Looking at the v_{yz} vector diagram corresponding to different herringbone widths ω_1 in Fig. S2, one can see that the larger values of v_{yz} only appear where the fluid enters and exits the herringbone. This is because when the fluid flows to the onset of the herringbone shape, it will flow upward and fill the herringbone-shaped groove; and then when it flows to the end of the herringbone, it will flow downward and exit the groove. Therefore, the v_{yz} value at the beginning and end of the herringbone channel is larger, while the velocity component perpendicular to the main flow direction is smaller for flow in the groove. When the width of the herringbone ω_1 is larger, the v_{yz} value in the middle of the herringbone channel is smaller. It is clear that if the herringbone channel's width ω_1 is too large, the number of vortices per unit length will be reduced. Therefore, the herringbone channel's optimal width is 100 μm.

At the same time, it can be seen from Fig. S1(b) that there is no obvious correlation between v_{yz} and the minimum element width ω when the herringbone width ω_1 is fixed. In order to facilitate fabrication, we must ensure the aspect ratio of the structure, and so the minimum unit width is set to be 3 times the height of the flow channel, that is, 150 μm.

3.2 Chip bottom structural design

The deterministic lateral displacement (DLD) principle refers to how when particles with different sizes flow through a microcolumn array, particles with a diameter larger than the critical diameter frequently collide with the column, and particles with a diameter smaller than the critical diameter follow the flow path. At present, this principle has been widely used to separate blood cells (Catarino et al., 2019), extracellular vesicles (Santana et al., 2014; Havers et al., 2023), submicron particles (Zhang et al., 2020), and nanoparticles (Xie et al., 2020). The application of this method in CTC capture can cause cells to collide with the bottom structure more frequently, thus increasing the probability of capture. Accordingly, a deterministic transverse displacement column was selected as the bottom structure of the circulating tumor cell capture chip in this study.

The design of the top herringbone-shaped microchannel causes the fluid to flow in a spiral pattern in the flow channel, and thus the design of the bottom structure should make the surface of the microcolumn be as perpendicular as possible to the

Unedited

velocity direction of the cells. Therefore, we opt to design the bottom microcolumn as a square column with a certain angle. High blockage tendency is a common problem in CTC capture based on the DLD principle. In order to reduce the probability of blockage, a column height of 20 μm was selected. Moreover, to simplify the design process, the column length was also set to 20 μm.

Currently, relevant studies on columns leveraging the DLD principle are relatively mature, and there is an empirical design formula for square columns (Zhang et al., 2015) as follows:

$$D_c = 1.4G\xi^{0.69} \quad (3)$$

where D_c is the critical diameter, G is the column spacing, and ξ is the tangent value of the offset angle. According to this formula, the spacing and deviation angle of the column array will affect the frequency of collisions between the particles and the bottom structure, so the spacing and deviation angle of the column array must be designed first. Since the average diameter of the human breast cancer cell MCF-7 used in subsequent experiments was 15 μm, the critical diameter was taken as this value. When the critical diameter is 15 μm, the relationship between column spacing and deviation angle is shown in Fig. 2(f). In order to prevent blockage, the maximum spacing was set to 60 μm, and the corresponding offset angle is 5°. The column shape is designed below, and the angle θ of the square column is designed first. The included angle range is 0°-100°, and the included angle gradient is 10°. The higher the collision frequency between CTCs and the bottom structure, the greater the probability of CTC capture. Therefore, the simulation design of the bottom structure was based on a selected collision frequency between the particles and the bottom structure, that is, the ratio of the number of collisions between the particles and the bottom structure, to the total number of particles. The relationship between the simulated column angle and the normalized collision frequency is shown in Fig. 2(f). It can be seen that with the increase of the square column angle, the collision frequency first increases and then decreases, so accordingly we take the angle of the square column as 70°.

For further design of the column shape, we considered changing the simple square column into a more complex three-dimensional structure. However, when meshing complex columns, very fine grids are needed to reflect the bottom structure more accurately, which makes calculations difficult. Thus, further design of the columns is instead informed by subsequent experiments.

3.3 Chip fabrication

Scanning electron microscope (SEM) and light microscope images of the PDMS after mold inversion are shown in Fig. 3(a) and Fig. 3(b), respectively. In Fig. 3(a), PDMS was placed on the 30° stage and sprayed with gold. The actual flow path height was twice the measured length, that is, 50 μm. It is clear that the microchannel size is basically consistent with the design size. At the same time, the mold remains intact after over ten cycles of mold reversal, and thus it can be seen that the aspect ratio of the structure is effective. The smaller aspect ratio enables the micro-convex portion of the mold to suffer less shear force during the mold reversal, making it more difficult for the microstructure to fall off.

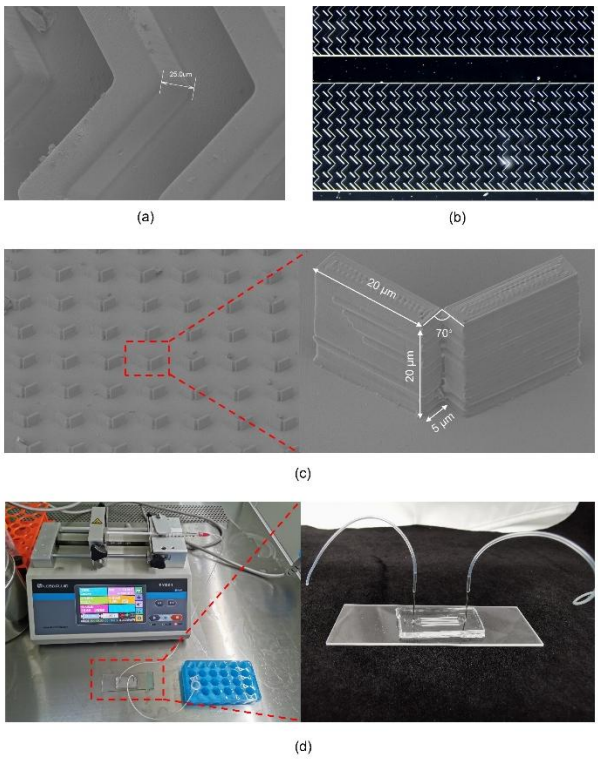

Fig. 3 Schematic diagram of the bottom and top of the chip. (a) The scanning electron microscope image of the top structure of PDMS after mold inversion; (b) Optical microscope image of the top structure after mold inversion; (c) SEM diagram of the bottom structure; (d)

Unedited

The operation of the CTC capture system.

The bottom structure was processed with two-photon polymerization, with the bottom microstructure revealed through SEM in Fig. 3(c). The complete assembled microfluidic chip and the system for CTC capture are shown in Fig. 3(d).

3.4 Chip performance characterization

The performance of the chip can mainly be described by capture rate, release rate, cell activity after release, and capture purity. The relationship between flow rate and capture rate was explored to determine the optimal flow rate for capture. As shown in Fig. 4(a), with the increase of flow velocity, the capture rate generally decreases. In order to maximize the processing flux of the chip and ensure an adequate capture rate of CTCs, the flow rate for subsequent capture experiments was selected as 1 mL/h.

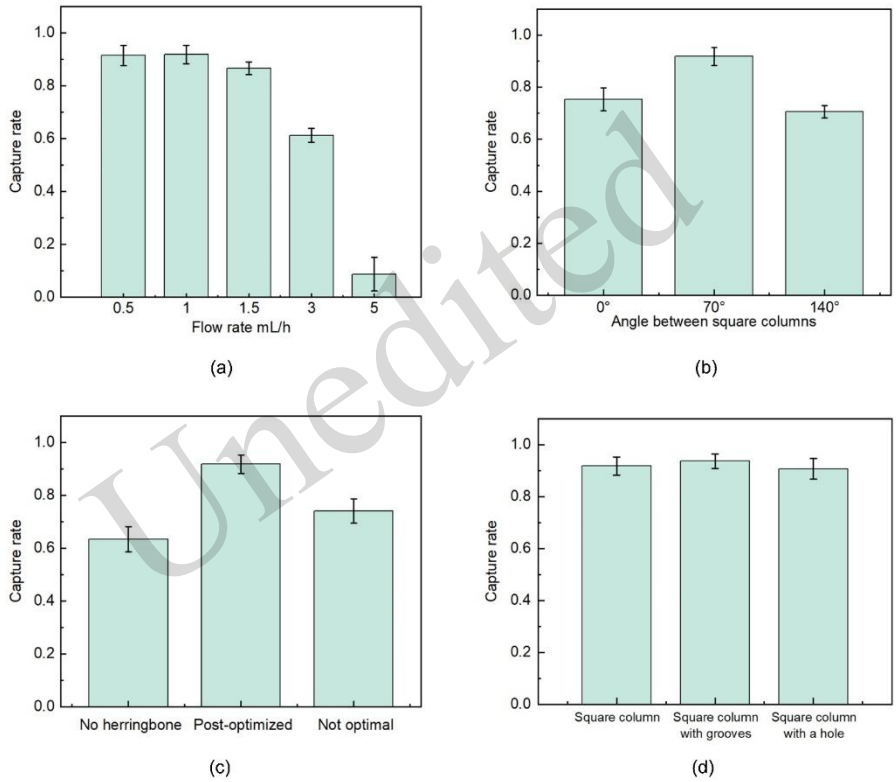

Fig. 4 (a) The relationship between flow rate and capture rate; (b) The relationship between the angle of the square column and the capture rate; (c) The capture rate corresponding to the chip with different top structures; (d) The capture rate of the chip with a different square column shape at the bottom. All the above results are expressed as the mean ± standard deviation from three independent experiments.

To verify the effectiveness of the design of the bottom structure, bottom columns with angles of 0°, 70°, and 140° were printed, and the herringbone-shaped microchannel designed in the previous section was used for three sets of capture experiments on the top of the three columns. The statistical capture rate is shown in Fig. 4(b). When the angle of the square column was 0°, the capture rate was about 75.37%; when the angle of the square column was 70°, the capture rate was around 91.87%; and when the angle of the square column was 140°, the capture rate was around 70.57%. As the angle of the square column increases, the capture rate first increases and then decreases, which is consistent with the simulation results. In order to verify the effectiveness of the top structure design, three groups of top structures were tested: one without a herringbone-shaped microchannel, one with a herringbone-shaped microchannel after simulation optimization, and one with a non-optimal

Unedited

herringbone-shaped microchannel with minimum element width of 150 μm and herringbone shape width of 50 μm. The bottom structures of the three groups were all 70° angle square columns following optimization. The capture rate of the three groups is shown in Fig. 4(c). The capture rate of MCF-7 is about 63.43% for the microfluidic chip using the top flow channel without a herringbone shape, and 74.13% for the microfluidic chip using the top flow channel with the minimum cell width of 150 μm and the herringbone shape width of 50 μm – these results are also consistent with the simulations.

Next, two more complex three-dimensional columns were printed for capture, and the influence of column shape on the capture rate was explored. To increase the effective area of the aptamer modification, four slots that were 2 μm wide, 20 μm long, and 2.5 μm deep were etched into the surface of the square column for the first type of column shape, as shown in Fig. S3(a). The second type of column makes a ball-shaped groove on the surface of the square column, as depicted in Fig. S3(b). The chip was assembled using the optimized top herringbone-shaped microchannel and the bottom structure composed of two derived cylindrical arrays, and the capture experiment was conducted on MCF7 cell suspension with a cell density of 1×10^3 /mL, with the results shown in Fig. 4(d). The capture rate of CTCs for the chip with the grooved square column at its bottom was about 93.70%, for the chip with the spherical hole square column it was about 90.80%, and for the chip with the simple square column it was about 91.87%. Therefore these more complex three-dimensional columns didn't have a significant effect on the capture rate.

The release of the trapped cells was then investigated. First, DNase treatment time and aptamer degradation rate were investigated using Cy5-labeled aptamers, so as to determine the optimal DNase treatment time for cell release. A 100 μm × 100 μm × 10 μm square array was printed and treated with DNase for 5, 10, 15, and 20 minutes after modification; the fluorescence intensity was then measured. As shown in Fig. 5(c), with the increase of DNA enzyme treatment time, the release efficiency of aptamer gradually increased, with the release rate reaching about 75.0% after an incubation time of 15 min, and then the increasing trend slowed as the incubation time increased further. To minimize the incubation time of cells in the DNase without nutrients, the subsequent DNase incubation time was set at 20 min. After the incubation, the captured MCF7 was released.

The fluorescence images before and after release are presented in Fig. 5(d). Statistically, the release rate was about 77.57%. The release rate to cells was slightly lower than that to aptamers. Theoretically, a single cell needs multiple pairs of antigens to bind to the aptamer in order to fix to the wall, so the release rate of DNase to the cell should be greater than that of the aptamer; however, the experimental results are contrary to this. The reasons for this may be as follows: first, a small number of cells adhere to the wall non-specifically, that is, they are not fixed on the wall by binding with the aptamer, so the aptamers decomposed through DNA enzymes cannot be released. Second, DNA enzymes may not fully degrade the aptamer into deoxyribonucleotides, but only degrade long aptamer chains into several short chains, and thus not completely separate the aptamer from the wall. For the fluorescent aptamer used in the DNase release experiment, the fluorophores are modified at its ends, and the degradation of any single chain can cause the fluorophores to break away from the wall and make the wall lose its red fluorescence, thus leading to the difference between the two groups of experiments.

Unedited

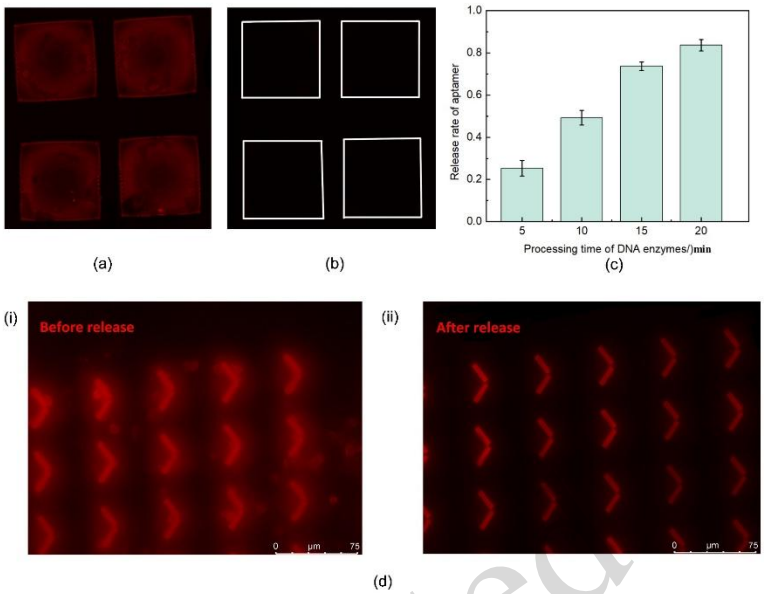

Fig. 5 DNA enzyme release effect and statistical diagram of the aptamer. (a) Fluorescence pattern of the anterior block treated by DNase; (b) The surface fluorescence of the block after 20 minutes of DNase treatment; (c) The relationship between DNase treatment time and aptamer release rate, where the results are expressed as the mean ± standard deviation from three independent experiments; (d) The fluorescence images of captured cells before and after release.

Subsequently, the cell activity after release was investigated. During the process of capture and release, the cell activity is affected by the following factors: digestion using pancreatin-free cellular digestive fluid, the shear process during capture, and the release of captured cells using DNA enzymes. Therefore, LIVE/DEAD staining was performed on the cells after the three processes, with the results presented in Fig. 6(a) and 6(b). It can be seen that the cell activity after digestion by pancreatin-free cell digestive fluid was about 77.47%, and the cell activity after capture and release was about 72.88%; therefore the relative activity of cells after capture and release was 94.08%. Moreover, it is clear that the 1 mL/h flow rate and the DNA enzymes had no significant effect on cell activity. After this experiment, the released cells were re-cultured, with the results demonstrating that the released cells were able to proliferate normally in the culture bottle.

Subsequently, about 1,000 /mL Cell Tracker red-labeled EpCAM negative cells K562 were used for capture experiments, with the captured cells shown in Fig. 6(c). According to the resulting statistics, the capture rate of K562 was 4.83%. Then, about 1000 /mL EpCAM-positive cells MCF7 and about 1000 /mL EpCAM-negative cells K562 were mixed in a ratio of 1:1 for capture. The fluorescence diagram of captured cells after rinsing is shown in Fig. 6(d). The captured MCF7 cells were observed with SEM at 45 degrees and from a top view Fig. 6(e). The capture rate of the two kinds of cells was statistically measured. One can observe that the capture rate for EpCAM-positive cells MCF7 was about 90.63%, the capture rate for EpCAM-negative cells was about 2.93%, and the capture purity was approximately 96.83%. Compared with the capture of a single cell, the capture rate of both cell types decreased in the mixed cell suspension. The data shows that the capture rate of positive MCF7 cells by the chip dropped from 91.87% to 90.63%. There may be two reasons for this decline in the capture rate of MCF7: first, K562, which experiences non-specific adhesion to the wall, occupies a position where MCF7 may be bound to the aptamer. Second, there is a collision between MCF7 and K562, which will affect the original movement of MCF7. Both of these factors will lead to a decrease in the contact frequency between MCF7 and the aptamer, thereby resulting in a lower capture rate. The reason for the lower capture rate of K562 may be that the aptamer-bound MCF7 occupies the non-specific binding position of K562. These results demonstrate that the proposed chip can

Unedited

be used for effective CTC capture with excellent sensitivity in complex cell mixture conditions; our methodology therefore shows promise for real blood flow scenarios with red and white blood cells.

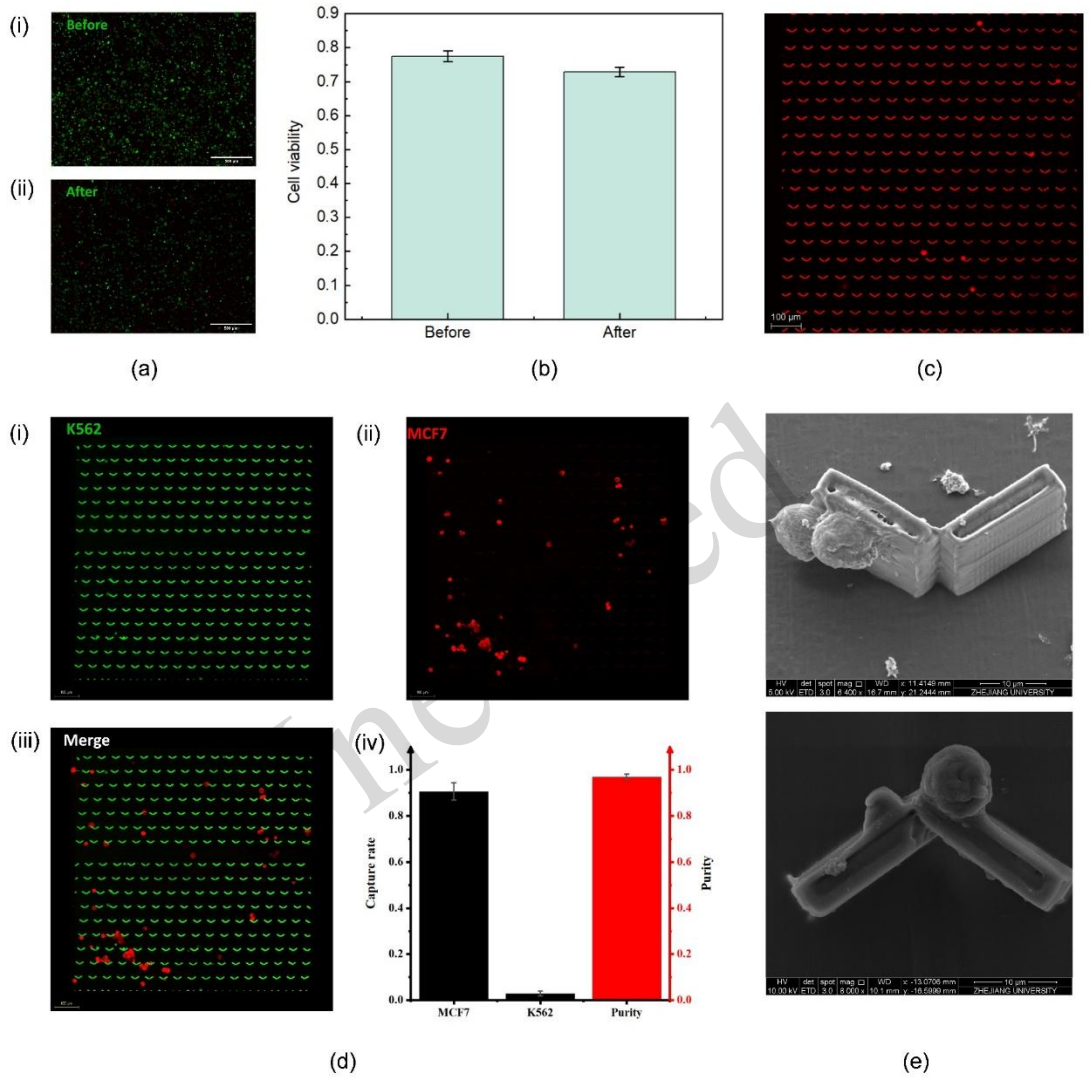

Fig. 6 (a) LIVE/DEAD staining images of pre-captured cells, where red represents dead cells, and green live cells (a-i); LIVE/DEAD staining images of the cells after capture and release (a-ii); (b) Statistical graphs of cell activity before and after capture and release; (c) The fluorescence images of EpCAM-negative cells captured by the chip; (d) The fluorescence images and statistical data of two kinds of cells captured by the bottom structure in the mixed cell suspension; (e) A scanning electron microscope image of the cells captured by the bottom structure. The results of (b) and (c) are expressed as the mean ± standard deviation from three independent experiments.

To better position the advancement of this work, the performance of our system is briefly compared with several state-of-the-art systems. For instance, our platform achieved a capture rate of 91.87%, which compares favorably with the 86.37% reported by Wu et al. (2023) – they used an dielectrophoresis based method involving inkjet printing of microelectrode arrays onto thin films (Wu, et al., 2023). The advantages of our method are particularly evident in terms of purity and release rate. For instance, compared with the functionalized nano-magic-clip capture chip based on the immune binding principle by Sun et al. (2022) (Sun et al., 2022), at a similar capture rate (89.9%), we achieved a capture purity of 96.83% and a release rate of 77.57% under mixed cell conditions. This is crucial for the effectiveness of CTC detection, which has rarely been explored in previous studies.

Additionally, maintaining the cell survival rate after the separation is an important issue that has not been fully addressed in earlier research. The relative viability of the cells released by our method is approximately 94.08%, while existing capture methods with high capture rates based on dielectrophoresis principles often bring along issues such as a relatively high electric field intensity in the microchannels, and the joule heating effect; these can cause irreversible damage to the cells and thereby affect the viability of the released cells. We primarily attribute the comprehensive performance enhancement shown in our study to the integration of the principle of immunoaffinity and deterministic lateral displacement technology. This design achieves a balance between the capture and release mechanisms, avoiding trade-offs between high purity, efficient release, and cell viability. Therefore, this comparison underscores that our methodology presents a balanced and effective solution, and pushes the limits of multiple key performance metrics.

However, to apply this technology in future clinical practice, it is imperative to improve upon the discrete and labor-intensive manual operation procedures. Therefore, a critical direction for our future work will be the development of a semi- or fully-automated, integrated platform that combines the steps of sample introduction, capture, purification, release, and subsequent analysis. This would significantly reduce operator-induced variability, improve reproducibility, shorten the time needed for analysis, and thereby facilitate potential liquid biopsy applications in clinical settings.

4 Conclusions

A novel circulating tumor cell (CTC) capture chip was designed through computational fluid dynamics simulations of structures with herringbone-shaped mixers and deterministic lateral displacement technology. Soft lithography and two-photon polymerization technology were used to complete the processing of the chip, and an aptamer was grafted inside the chip for specific capture of CTCs. The capture rate of human breast cancer cell MCF7 was about 91.87%, the release rate was about 77.57%, and the relative activity of the cells after release was approximately 94.08%; the capture rate of negative human chronic myeloid leukemia cell line K562 was about 4.83%, and the capture purity of positive cells in the presence of mixed cells was approximately 96.83%. Our results demonstrated that the proposed CTC capture chip can achieve high capture rate, high purity, and high activity enrichment of CTCs, thus providing an effective platform for CTC detection and diagnosis. With future advancements in integration and automated development, this method may be impactful in clinical practice.

Acknowledgments

The authors would like to thank the funding supported by State Key Laboratory of High-performance Precision Manufacturing under Grant No. HPMKF202412, Zhejiang Provincial Natural Science Foundation of China under Grant No. LZ25E050001, The National Natural Science Foundation of China No. 52275294, Zhejiang Province's 2025 'Pioneer Leading Swan + X' Science and Technology Program No.2025C02122.

Author contributions

X.L. and C.Q. did most of the experiment, write the manuscript. K.L., A.R., J.H., W.L. and L.K. did some of the experiment and help for data analysis, M.Y, Z.W, X.J. discussed and edited the manuscript; H.Y provided the resources; X.X and L.M. supervised the manuscript process, review and edited the manuscript.

Conflict of interest

The authors declare no conflict of interest.

References

Alix-Panabières C, Pantel K, 2014. Opinion challenges in circulating tumour cell research. *NATURE REVIEWS CANCER*, 14(9):623-631. https://doi.org/10.1038/nrc3820

Antfolk M, Kim SH, Koizumi S, et al., 2017. Label-free single-cell separation and imaging of cancer cells using an integrated microfluidic system. *SCIENTIFIC REPORTS*, 7 https://doi.org/10.1038/srep46507

Catarino SO, Rodrigues RO, Pinho D, et al., 2019. Blood cells separation and sorting techniques of passive microfluidic devices: From fabrication to applications. *MICROMACHINES*, 10(9) https://doi.org/10.3390/mi10090593

Chaffer CL, Weinberg RA, 2011. A perspective on cancer cell metastasis. *SCIENCE*, 331(6024):1559-1564. https://doi.org/10.1126/science.1203543

Chen S, Chen J, Qin Z, et al., 2024. Microfluidic thermotaxic selection of highly motile sperm and in vitro fertilization.

Unedited

BIO-DESIGN AND MANUFACTURING, 7(5):687-700. https://doi.org/10.1007/s42242-024-00306-1

Cohen SJ, Alpaugh RK, Gross S, et al., 2006. Isolation and characterization of circulating tumor cells in patients with metastatic colorectal cancer. *CLINICAL COLORECTAL CANCER*, 6(2):125-132. https://doi.org/10.3816/CCC.2006.n.029

Cortés-Hernández LE, Eslami-S Z, Pantel K, et al., 2020. Molecular and functional characterization of circulating tumor cells: From discovery to clinical application. *CLINICAL CHEMISTRY*, 66(1):97-104. https://doi.org/10.1373/clinchem.2019.303586

Cristofanilli M, Budd GT, Ellis MJ, et al., 2004. Circulating tumor cells, disease progression, and survival in metastatic breast cancer. *NEW ENGLAND JOURNAL OF MEDICINE*, 351(8):781-791. https://doi.org/10.1056/NEJMoa040766

De Bono JS, Scher HI, Montgomery RB, 2009. Circulating tumor cells predict survival benefit from treatment in metastatic castration-resistant prostate cancer (vol 14, pg 6302, 2008). *CLINICAL CANCER RESEARCH*, 15(4):1506-1506.

Galletti G, Sung MS, Vahdat LT, et al., 2014. Isolation of breast cancer and gastric cancer circulating tumor cells by use of an anti her2-based microfluidic device. *LAB ON A CHIP*, 14(1):147-156. https://doi.org/10.1039/c3lc51039e

Havers M, Broman A, Lenshof A, et al., 2023. Advancement and obstacles in microfluidics-based isolation of extracellular vesicles. *ANALYTICAL AND BIOANALYTICAL CHEMISTRY*, 415(7):1265-1285. https://doi.org/10.1007/s00216-022-04362-3

Hu J, Ren A, Lv W, et al., 2025. Multiphoton polymerization-based micro/nanomanufacturing toward precision medicine. *Engineering*, 49:35-60. https://doi.org/https://doi.org/10.1016/j.eng.2024.10.016

Kang H, Xiong Y, Ma L, et al., 2022. Recent advances in micro-/nanostructure array integrated microfluidic devices for efficient separation of circulating tumor cells. *RSC Advances*, 12(54):34892-34903. https://doi.org/10.1039/D2RA06339E

Kang H, Li C, Liu W, et al., 2025. Si nanorod array integrated microfluidic device for enhanced extracellular vesicle isolation. *Advanced Materials Technologies*, 10(1):2400294. https://doi.org/https://doi.org/10.1002/admt.202400294

Kang YT, Doh I, Byun J, et al., 2017. Label-free rapid viable enrichment of circulating tumor cell by photosensitive polymer-based microfilter device. *THERANOSTICS*, 7(13):3179-3191. https://doi.org/10.7150/thno.19686

Li CA, Chen TN, 2005. Simulation and optimization of chaotic micromixer using lattice boltzmann method. *SENSORS AND ACTUATORS B-CHEMICAL*, 106(2):871-877. https://doi.org/10.1016/j.snb.2004.09.006

Li HX, Qiao Y, Dai XL, et al., 2024. 3d bioprinting of tumor models and potential applications. *BIO-DESIGN AND MANUFACTURING*, 7(6):857-888. https://doi.org/10.1007/s42242-024-00317-y

Lin Y, He D, Wu Z, et al., 2023. Junction matters in hydraulic circuit bio-design of microfluidics. *BIO-DESIGN AND MANUFACTURING*, 6(1):38-50. https://doi.org/10.1007/s42242-022-00215-1

Liu Q, Mille LS, Villalobos C, et al., 2023. 3d-bioprinted cholangiocarcinoma-on-a-chip model for evaluating drug responses. *BIO-DESIGN AND MANUFACTURING*, 6(4):373-389. https://doi.org/10.1007/s42242-022-00229-9

Liu XS, Ma L, Yan WY, et al., 2022. A review of recent progress toward the efficient separation of circulating tumor cells via micro-/nanostructured microfluidic chips. *VIEW*, 3(1) https://doi.org/10.1002/VIW.20210013

Low WS, Abas WaW, 2015. Benchtop technologies for circulating tumor cells separation based on biophysical properties. *BIOMED RESEARCH INTERNATIONAL*, 2015 https://doi.org/10.1155/2015/239362

Ma L, Yang H, 2023. What's next toward the bio-design and manufacturing field? *BIO-DESIGN AND MANUFACTURING*, 6(6):735-741. https://doi.org/10.1007/s42242-023-00260-4

Park ES, Jin C, Guo Q, et al., 2016. Continuous flow deformability-based separation of circulating tumor cells using microfluidic ratchets. *SMALL*, 12(14):1909-1919. https://doi.org/10.1002/smll.201503639

Renier C, Pao E, Che J, et al., 2017. Label-free isolation of prostate circulating tumor cells using vortex microfluidic technology. *NPJ PRECISION ONCOLOGY*, 1 https://doi.org/10.1038/s41698-017-0015-0

Rosenberg R, Gertler R, Friederichs J, et al., 2002. Comparison of two density gradient centrifugation systems for the enrichment of disseminated tumor cells in blood. *CYTOMETRY*, 49(4):150-158. https://doi.org/10.1002/cyto.10161

Salafi T, Zhang Y, Zhang Y, 2019. A review on deterministic lateral displacement for particle separation and detection. *NANO-MICRO LETTERS*, 11(1) https://doi.org/10.1007/s40820-019-0308-7

Santana SM, Antonyak MA, Cerione RA, et al., 2014. Microfluidic isolation of cancer-cell-derived microvesicles from hetergeneous extracellular shed vesicle populations. *BIOMEDICAL MICRODEVICES*, 16(6):869-877. https://doi.org/10.1007/s10544-014-9891-z

Sarioglu AF, Aceto N, Kojic N, et al., 2015. A microfluidic device for label-free, physical capture of circulating tumor cell clusters. *NATURE METHODS*, 12(7):685-+. https://doi.org/10.1038/NMETH.3404

Sheng WA, Chen T, Tan WH, et al., 2013. Multivalent DNA nanospheres for enhanced capture of cancer cells in microfluidic devices. *ACS NANO*, 7(8):7067-7076. https://doi.org/10.1021/nn4023747

Shi JJ, Zhao CQ, Shen MQ, et al., 2022. Combination of microfluidic chips and biosensing for the enrichment of circulating tumor cells. *BIOSENSORS &*

Uncorrected

BIOELECTRONICS, 202 https://doi.org/10.1016/j.bios.2022.114025

Shu Y, Li B, Ma HL, et al., 2024. Three-dimensional breast cancer tumor models based on natural hydrogels: A review. *JOURNAL OF ZHEJIANG UNIVERSITY-SCIENCE B*, 25(9):736-755. https://doi.org/10.1631/jzus.B2300840

Smerage JB, Barlow WE, Hortobagyi GN, et al., 2014. Circulating tumor cells and response to chemotherapy in metastatic breast cancer: Swog s0500. *JOURNAL OF CLINICAL ONCOLOGY*, 32(31):3483-+. https://doi.org/10.1200/JCO.2014.56.2561

Stroock AD, Dertinger SKW, Ajdari A, et al., 2002. Chaotic mixer for microchannels. *SCIENCE*, 295(5555):647-651. https://doi.org/10.1126/science.1066238

Sun N, Yang Y, Miao H, et al., 2022. Discovery and characterization of circulating tumor cell clusters in neuroendocrine tumor patients using nanosubstrate-embedded microchips. *Biosensors and Bioelectronics*, 199:113854. https://doi.org/https://doi.org/10.1016/j.bios.2021.113854

Sung H, Ferlay J, Siegel RL, et al., 2021. Global cancer statistics 2020: Globocan estimates of incidence and mortality worldwide for 36 cancers in 185 countries. *CA-A CANCER JOURNAL FOR CLINICIANS*, 71(3):209-249. https://doi.org/10.3322/caac.21660

Varmazyari V, Habibiyan H, Ghafoorifard H, et al., 2022. A dielectrophoresis-based microfluidic system having double-sided optimized 3d electrodes for label-free cancer cell separation with preserving cell viability. *SCIENTIFIC REPORTS*, 12(1) https://doi.org/10.1038/s41598-022-16286-0

Wu MR, Gao Y, Luan QY, et al., 2023. Three-dimensional lab-on-a-foil device for dielectrophoretic separation of cancer cells. *ELECTROPHORESIS*, 44(23):1802-1809. https://doi.org/10.1002/elps.202200287

Wu MX, Huang PH, Zhang R, et al., 2018. Circulating tumor cell phenotyping via high-throughput acoustic separation. *SMALL*, 14(32) https://doi.org/10.1002/smll.201801131

Xiang N, Wang J, Li Q, et al., 2019. Precise size-based cell separation via the coupling of inertial microfluidics and deterministic lateral displacement. *ANALYTICAL CHEMISTRY*, 91(15):10328-10334. https://doi.org/10.1021/acs.analchem.9b02863

Xie YL, Rufo J, Zhong RY, et al., 2020. Microfluidic isolation and enrichment of nanoparticles. *ACS NANO*, 14(12):16220-16240. https://doi.org/10.1021/acsnano.0c06336

Yu XL, He RX, Li SS, et al., 2013. Magneto-controllable capture and release of cancer cells by using a micropillar device decorated with graphite oxide-coated magnetic nanoparticles. *SMALL*, 9(22):3895-3901. https://doi.org/10.1002/smll.201300169

Zeming KK, Ranjan S, Zhang Y, 2013. Rotational separation of non-spherical bioparticles using i-shaped pillar arrays in a microfluidic device. *Nature Communications*, 4 https://doi.org/10.1038/ncomms2653

Zhang NA, Deng YL, Tai QD, et al., 2012. Electrospun tio2 nanofiber-based cell capture assay for detecting circulating tumor cells from colorectal and gastric cancer patients. *ADVANCED MATERIALS*, 24(20):2756-2760. https://doi.org/10.1002/adma.201200155

Zhang TL, Hong ZY, Tang SY, et al., 2020. Focusing of sub-micrometer particles in microfluidic devices. *LAB ON A CHIP*, 20(1):35-53. https://doi.org/10.1039/c9lc00785g

Zhang YZ, Wang ZY, Wu L, et al., 2018. Combining multiplex sers nanovectors and multivariate analysis for in situ profiling of circulating tumor cell phenotype using a microfluidic chip. *SMALL*, 14(20) https://doi.org/10.1002/smll.201704433

Zhang ZM, Henry E, Gompper G, et al., 2015. Behavior of rigid and deformable particles in deterministic lateral displacement devices with different post shapes. *JOURNAL OF CHEMICAL PHYSICS*, 143(24) https://doi.org/10.1063/1.4937171

Zhou JH, Rossi J, 2017. Aptamers as targeted therapeutics: Current potential and challenges. *NATURE REVIEWS DRUG DISCOVERY*, 16(3):181-202. https://doi.org/10.1038/nrd.2016.199

Electronic supplementary materials

Figs. S1–S3

中文概要

题　目： 一种基于双光子聚合的结合人字形微通道和确定性横向位移原理的微流控芯片用于循环肿瘤细胞的高效捕获

作　者： 梁心怡[1,2]，秦昌玮[1,2]，李凯强[3]，任安[1,2]，胡家睿[1,2]，吕为康[1,2]，柯路南[1,2]，王震[3]，俞梦飞[4]，江秀秀[5]，杨华勇[1,2]，许晓斌[6]，马梁[1,2]

机　构： [1]浙江大学，流体动力基础件与机电系统全国重点实验室，中国杭州，310058；[2]浙江大学，机械工程学院，中国杭州，310058；[3]浙江省人民医院输血内科变态反应中心检验医学中心，杭州医学院附属人民医院，中国杭州，310014；[4]浙江大学医学院附属口腔医院，中国杭州，310003；[5]浙江省妇科临床研究中心，浙江省母婴健康重点实验室，浙江大学医学院附属妇女医院计划生育科，中国杭州，310006；[6]同济大学材料科学与工程学院，中国上海，201804

Unedited

目　的：循环肿瘤细胞（CTC）的富集和检测对肿瘤转移复发评估、疗效监测和用药指导至关重要，但现有方法难以兼顾高捕获率和高纯度。本文旨在开发一种微流控芯片，通过结合人字形微流道和确定性横向位移技术，实现循环肿瘤细胞的高捕获率、高纯度和高活性富集与释放。

创新点：1. 提出结合人字形微流道和确定性横向位移技术的微流控芯片设计，基于免疫结合原理，通过结构优化提高细胞与适体的接触频率，从而提升捕获率；2. 利用适体对肿瘤细胞表面抗原的特异性实现高纯度捕获，并通过 DNA 酶消化适体实现细胞的高活性释放；3. 采用计算流体力学仿真和双光子聚合打印技术，实现对芯片结构的精确设计与制作。

方　法：1. 通过计算流体力学仿真，优化芯片顶部人字形微流道的间距、槽宽和单元宽度，以及底部确定性横向位移柱列的柱形设计，以提高流场效率和细胞碰撞频率（图 2 和 4）；2. 采用软光刻技术加工顶部结构，并探索双光子聚合打印工艺制作底部结构，通过键合组装和适体修饰，确定最佳修饰浓度和流速承载能力（图 3 和 5）；3. 通过实验表征芯片性能：确定最佳捕获流速，验证结构优化有效性，测试释放后细胞活性和增殖能力，评估阴性细胞捕获率和混合细胞中阳性细胞捕获纯度（图 6）。

结　论：1. 芯片实现了对循环肿瘤细胞的高效捕获（MCF7 细胞捕获率约 91.87%）、高活性释放（释放率约 77.57%，细胞相对活性约 94.08%），以及高纯度富集（对 K562 阴性细胞捕获率约 4.83%，混合细胞中阳性细胞捕获纯度约 96.83%）；2. 结合人字形微流道和确定性横向位移技术的设计，通过仿真优化有效提高了捕获性能。

关键词：循环肿瘤细胞；细胞分选；微流控芯片

Unedited